



Supporting Online Material for
**Complex Patterning by Vertical Interchange Atom Manipulation Using
Atomic Force Microscopy**

Yoshiaki Sugimoto, Pablo Pou, Oscar Custance,* Pavel Jelinek, Masayuki Abe,
Ruben Perez, Seizo Morita

*To whom correspondence should be addressed. E-mail: custance.oscar@nims.go.jp

Published 17 October 2008, *Science* **322**, 413 (2008)
DOI: 10.1126/science.1160601

This PDF file includes:

Materials and Methods
Figs. S1 to S8
References

Supporting Online Material: Complex patterning by vertical interchange atom manipulation using atomic force microscopy

Yoshiaki Sugimoto,¹ Pablo Pou,² Oscar Custance,^{3*}
Pavel Jelinek,⁴ Masayuki Abe,^{1, 5} Ruben Perez,² Seizo Morita¹

¹Graduate School of Engineering, Osaka University, 2-1 Yamada-Oka, 565-0871 Suita,
Osaka, Japan

²Departamento de Física Teórica de la Materia Condensada, Universidad Autónoma de Madrid,
28049 Madrid, Spain

³National Institute for Materials Science, 1-2-1 Sengen, 305-0047 Tsukuba,
Ibaraki, Japan

⁴Institute of Physics, Academy of Sciences of the Czech Republic, Cukrovarnicka 10,
1862 53 Prague, Czech Republic

⁵PRESTO, Japan Science and Technology Agency, 332-0012 Saitama, Japan

* To whom correspondence should be addressed: custance.oscar@nims.go.jp

1 Materials and Methods.

1.1 Experimental methods.

The experiments were performed in ultrahigh vacuum using an atomic force microscope (AFM) operated in dynamic mode under the frequency modulation detection scheme (*I*), keeping the cantilever oscillation amplitude constant. In our experiments, we apply a bias voltage between tip and sample to cancel the tip-surface contact potential difference, in order to minimize the long-range electrostatic interaction. In this operation mode, our main observable is the frequency shift (the shift of the first mechanical resonant frequency of the cantilever to lower values due to forces acting on the tip). Scanning the surface keeping the frequency shift constant gives access to topographic images of the surface, adjusting the feedback parameters to

obtain a minimal error of the frequency shift signal with respect to the topographic set point. In every moment, we also record the cantilever oscillation amplitude —to corroborate that is kept constant— and the dissipation signal (the additional amount of energy we have to put into the oscillating cantilever to keep the oscillation amplitude constant under the presence of non-conservative tip-surface interactions).

We have used commercial silicon cantilevers with a sharp Si tip at the cantilever’s free end (POINTPROBE- Silicon SPM-Sensor, NCLR-W, from Nanoworld, Switzerland). Prior experiment, a new cantilever tip was prepared by ion Ar sputtering with an ion energy of 0.6 keV, adjusting the partial pressure of Ar to get an ion current of $0.2 \mu\text{A}$ measured at the cantilever holder, and setting the sputter time to obtain reactive yet sharp tips giving high quality atomic resolution images (the sputter time must be calibrated for each cantilever wafer). Sometimes, slight contacts with the surface are required to improve atomic resolution image quality or to stabilize the tip after modifications in force spectroscopy measurements. If the tip was producing stable imaging and good force spectroscopy data, it was used over several measurements sessions without any further cleaning treatment.

Samples were produced by thermal evaporation a ~ 0.37 monolayers of Sn —one monolayer is defined as the atomic density of the Si(111) surface— of Sn atoms over a clean Si(111)-(7x7) surface thermalized to room temperature, and subsequent ohmic annealing of the Sb-doped silicon substrate at 650° typically for 2 minutes. This procedure provides high quality Sn/Si(111)-($\sqrt{3} \times \sqrt{3}$)R30° surfaces with a low density of defects (2, 3).

Room-temperature force spectroscopy acquisition was performed by recording the frequency shift, the oscillation amplitude and the dissipation signal upon a single tip-surface approach and retraction cycle on top of the probed surface atom, keeping the relative tip-surface lateral position with a precision better than $\pm 0.1 \text{ \AA}$ (4).

The protocol we have followed to identify and reproduce the vertical atom interchange processes reported here is to perform force spectroscopic measurements driving the tip successively closer to the surface until it is determined the threshold tip-surface distance in which instabili-

ties in the frequency shift signal occur. After imaging the surface and checking that a vertical atomic interchange has taken place, force spectroscopy measurements exploring a tip-surface distance range from the free-oscillation region (absence of tip-surface interaction) to this threshold distance were successively performed over the same atomic position or at different surface locations (Figs. S1, S2 and S5). When a set of forward and backward curves is measured before reaching this threshold distance, the curve upon retraction matches —within the experimental noise — the one acquired during the approach.

1.2 Calculation of the experimental short-range force from the frequency shift.

Force spectroscopy using Frequency Modulation AFM (5) allows us to quantify very precisely the tip-surface interaction forces. In our experiments, these interactions are the long-range electrostatic and van der Waals forces, and the short-range chemical force between the tip-surface closest atoms (6), which is the relevant interaction for atomic resolution imaging. While our main observable is the frequency shift, the total force acting on the cantilever tip —including both long and short range interactions— can be obtained through the so-called inversion procedures: a mathematical operation over the spectroscopic data based in the inversion of the equation that relates frequency shift and tip-surface interaction forces (7–10).

The short-range interaction forces shown in Figs. S1 and S2 were obtained from the corresponding frequency shift signals by applying the inversion procedure described in Ref. 10 and the subsequent subtraction of the long-range contributions to the total force as described in Ref. 6. In the calculation of the force characteristics displayed in Figs. S1 and S2, the points of the frequency shift corresponding to the instability associated with the vertical atomic interchange were excluded, as the mathematical relation between the frequency shift and the tip-surface interaction force (8, 10) is not well defined at the instability.

1.3 First-principles simulations.

Our calculations are based on density functional theory implemented with a local orbital basis using the FIREBALL code (11). The details of the basis set we used are described elsewhere (3). To model the surface we have considered a (6×6) periodic slab that includes six Si layers with H saturating the dangling bonds at the deeper layer. Only the Γ point was included in the sampling of the Brillouin zone. The tip-surface interaction energy was determined in a stepwise, quasi-static manner by approaching the tip parallel to the surface. At each step, the atoms in the slab and the tip model were allowed to relax to their ground-state configuration with convergence criteria for the total energy and forces of 10^{-6} eV and 0.05 eV \AA^{-1} . The Si and H layers at the bottom of the surface slab were fixed during the relaxation process.

1.4 Calculation of energy barriers: the Nudged Elastic Band method.

The nudged elastic band (NEB) (12) is a well-established method for finding transition paths and the corresponding energy barriers between given initial and final states. Using this method, the Minimum Energy Path (MEP) between these two states can be calculated. Any maximum along the MEP is a saddle point on the potential energy surface, and the energy of the highest saddle point gives the activation energy needed for the transition.

Briefly, the method works as follows (13): A collection of intermediate sets of atomic configurations (or images) is created by a straight line interpolation of the coordinates of the atoms from the initial to the final state. Those images are connected together with springs to form a chain that provides a discrete representation of the path from the initial to the final state. This chain mimics an elastic band made of beads (the images) and springs.

The total energy of the entire chain has to be minimized to find the MEP. This total energy includes both the sum of the total energies of the different images and the contribution from the harmonic interaction between neighboring images along the direction of the path described by the chain. The minimization process involves the relaxation of the coordinates of the atoms in the different images subject to the constraints imposed by the springs. In order to avoid the

elastic band to cut corners (getting pulled off the MEP) and the images to slide down towards the initial and final states, the forces on the atoms are modified such that the original forces parallel to the path and the inter-image spring forces perpendicular to the path are removed (this is referred to as path "nudging"). Thus, once the entire chain is relaxed as a unit, the MEP is revealed. Notice that, proceeding in this way, the forces perpendicular to the optimized transition path are minimal, a characteristic property of the MEP. The sets of atomic configurations that the system explores between the initial and final states through the MEP are what we call in Fig. 4 "Reaction coordinate".

In our calculations of the typical energy barriers involved in vertical atom interchange processes (Fig. 4), we have used nine "images" —including the initial and final states labelled as α and β , respectively— of which a zoom of the final relaxed structures over the relevant region of the tip-surface interface is displayed in Fig. 4C. As described above, the initial set of atomic configuration correspond to a simple linear interpolation between the structures of the initial and final states. Figure 4B displays the final energies for the sets of different atomic configurations defining the MEP for the transition of the system from an energy branch resulting in a Sn deposition to the one associated with the concerted vertical interchange (see Fig. 4C) for details about the local bonding structure of the tip-surface interface.

1.5 Calculation of the frequency shift at finite temperature from the theoretical force curves when the system shows force hysteresis.

The calculation of the frequency shift when the system presents force hysteresis in an approach-retraction cycle is easy to carry out at zero temperature once the approach and retraction solutions are known (14, 15). However, at finite temperature, the thermal energy can induce the system to jump over energy barriers between different solutions (16). To include the effect of the temperature, it is necessary to know the energy barriers for the transition between relevant solutions for a wide range of tip-surface distances. Reference 15 discusses how to calculate the frequency shift for a system evolving between two solutions, A and B, during the approach-retraction cycle. Assuming that the tip oscillates sinusoidally $z(t) = z_0 + A_0 \sin(\omega t)$, the

frequency shift is obtained from:

$$\omega^2 - \omega_0^2 = -\frac{\omega}{\pi A_0 M} \int_0^{2\pi/\omega} F_{eff}(t) \sin(\omega t) dt \quad (1)$$

where, z_0 is the mean cantilever-surface separation, ω is the oscillation frequency, ω_0 is the first mechanical resonance frequency of the free cantilever, A_0 is the oscillation amplitude, M is the cantilever effective mass and $F_{eff}(t)$ is the force between the tip and the surface as a function of the time. This force is given by:

$$F_{eff}(t) = P_A(t)F_A(z) + [1 - P_A(t)]F_B(z), \quad (2)$$

being $F_A(z)$ the force felt by the tip when the system evolves following the solution A, and $F_B(z)$, the force for the solution B. $P_A(t)$ and $[1 - P_A(t)]$ measures the probability of the system to be in the state A or in the state B, respectively, at the time t . These probabilities are determined by the energy barriers between A and B, that depend on the tip-surface distance.

For the system considered in this work, the complexity of the phase space requires the use of non-trivial approaches (such as the NEB method discussed above) to calculate these transition barriers for the relevant range of tip-surface distances. Given the system size, each of these calculations is difficult and very computationally demanding, even for our fast first-principles methods. Thus, the complete characterization of the potential energy surfaces as a function of the distance at the ab initio level is simply out of reach. However, the qualitative effect of the temperature can be included making basic assumptions about the probability $P_A(t)$. We have approached it with a Fermi function. The parameters have been fitted to produce effective forces for approach and retraction (see eq. 2) that yield a dissipation energy close to the maximum value measured at the closest tip-surface distances in the experiments (1.2 eV, see Fig. S1). The resulting probabilities, shown in the inset of Fig. S3B, reproduce the basic behaviour found in previous studies (16), and provide the basis for our qualitative discussion on the presence of a double-well structure in the experimental force curves with similar maximum attractive force values in both minima (see section 2.3).

2 Discussion of spectroscopic data associated with vertical interchange atom manipulations in Sn/Si(111).

2.1 Forces and dissipation signal during the vertical atom interchange processes.

Figure S1 shows the variation of the frequency shift (raw data), the short-range interaction force, the cantilever oscillation amplitude, and the energy dissipated from the cantilever per oscillation cycle as a function of the tip-sample relative displacement, magnitudes simultaneously recorded upon a single approach and retraction cycle corresponding to the Sn deposition process (Fig. S1A) and the Si deposition process (Fig. S1B) shown in Figs. 1A and 1B, respectively.

The force characteristics displayed in Figs. S1A and B provide information about tip-apex modifications associated with the vertical interchange of atoms. In the Sn deposition shown in Fig. S1A, the resemblance between the shape of the approach and retraction curves both in the frequency shift and in the short-range force, together with the faint variation of the topographic signal before and after the interchange (see the profiles in Fig. S1C), point towards a negligible alteration of the tip-apex structure. On the contrary, in the Si deposition shown in Fig. S1B, while the force curve upon approach is almost identical to the retraction curve in Fig. S1A (see the inset plot), both frequency shift and short-range force differ completely upon retraction. This disparity between approach and retraction curves indicates a considerable modification of the tip-apex structure after the instability associated with the atomic interchange, which is confirmed by an important reduction in the topographic contrast for the image acquired just after the Si deposition, quantified in the profiles depicted in Fig. S1C. The fact that it is possible to easily recover almost the same initial resolution in topography—as it is shown in Fig. S1C—by scanning at slightly closer tip-surface distances in a nearby region suggests the formation of a metastable yet still reactive tip apex structure after a Si deposition from the tip. Corroboration of this behavior by the first-principles simulations performed in this work can be found in section 2.3.

2.2 Reproducibility of alternate vertical interchange atom manipulations.

Figure S2 shows the variation of the frequency shift and the corresponding short-range forces as a function of the relative tip-sample distance of alternate vertical interchange atom manipulations similar to the ones displayed in Fig. 1, but performed with a different cantilever tip and an elapsed time of almost two months between them.

Although the manipulations shown in Fig. S2 were performed in a separate measurement session with a different cantilever, the resemblance of the curves in both experiments is remarkable. Notice that all of the frequency shift curves shown in this work are raw data, displayed as recorded during the experiment; each curve corresponds to a single spectroscopic characteristic, and no accumulation of curves and further averaging was performed during either acquisition or analysis and representation.

This close agreement between curves points towards a tip-apex structure relatively frequently obtained in the experiments. It is also astonishing the similarity between curves for the substitution of a surface Si atom with a Sn atom coming from the tip (Fig. S2A and C), and the curves for the substitution of Sn atoms at the surface with a Si atom coming from the tip [Fig. S2B and D], suggesting a common mechanism for the manipulation processes in each case.

2.3 Understanding the basic features in the experimental short-range force curves.

The frequency shift curves measured for different vertical interchange atom manipulations are remarkably similar (see Figs. S1 and S2). Given this reproducibility, the experimental short-range forces should contain information about the atomistic processes involved in the vertical atom interchange. A characteristic feature in the experimental force curves is a double well structure at close tip-surface distances with similar maximum attractive forces in both minima (Figs. S1 and S2), that seems to develop in parallel with a significant increase in the dissipation signal (see Fig. S1). The presence of energy dissipation clearly indicates that the forces

involved are non-conservative, and therefore, hysteresis in the tip-surface interaction force for each oscillation cycle is expected (14, 16, 17).

Since the frequency shift is proportional to an average of the tip-surface interaction force over a cantilever oscillation cycle (7–9), any trace of different force solutions upon approach and retraction is lost when obtaining the tip-surface interaction force from the frequency shift (16, 17). However, the shape of the measured force will be determined by the energy barriers for the transitions between the energy branches that produce these different force solutions, in a stochastic process driven by the available thermal energy; these energy barriers dictate where the system jumps between the different solutions for a given tip-surface distance (16, 17). The energy landscape associated with these vertical atomic interchange processes provides an explanation for the intriguing features exhibited by the experimental short-range force curves, and it shows that the double well structure is produced due to a marked force hysteresis reflecting strong atomic rearrangements at the contact area.

In the approach curves shown in Fig. S1B, and Figs. S2B and S2D, there is no vertical atomic interchange before reaching the point of maximum proximity between tip and surface, and therefore the initial and final configuration upon approach and retraction before this point are identical. We could simulate this situation over one oscillation cycle by assuming that (i) the tip approaches the surface following energy branch C in Fig. 2; (ii) at a given tip-surface distance (C_3), the system jumps to the energy branch D; and (iii) upon retraction the system jumps back (D_2) to the branch C instead of branch A. The forces upon approach (squares) and retraction (circles) assuming these transitions between energy branches are shown in Fig. S3A. These jumps between energy solutions clearly lead to force hysteresis and to a dissipated energy of ~ 7 eV. The normalized frequency shift that would correspond to an approach and retraction cycle considering these two force solutions is shown in Fig. S3B (dashed line). The influence of the hysteresis is reflected in the expected step-like change at the tip-surface distance where the atom reallocations take place (14). The same inversion procedure used for the experimental curves (10) can be applied to this frequency shift curve for obtaining an estimation of the

expected measured force associated with these two force solutions, yielding the curve shown in Fig. S3A as a green dashed line. This curve coincides with the force of the C branch before the jump (up to this point, the force over the oscillation cycle is conservative), but, for closer distances, a strong hysteresis (jump) appears and the short-range force calculated from the frequency shift inversion loses its meaning (7–9).

This force curve is still quite different from the experimental ones, the main reason being that the experiments are performed at room temperature, and therefore, the system can relatively easily overcome energy barriers between different energy solutions. These thermally activated transitions smear out the steps and reduce the dissipation signal found at zero temperature (16). In order to incorporate the effect of the temperature, we have calculated the normalized frequency shift using the force solutions upon approach and retraction shown in Fig. S3A, but giving them relative probabilities (see the inset of Fig. S3B) in order to reproduce the measured dissipation energy (~ 1.2 eV/cycle) at the closest approach, (see section 1.5 for details). This normalized frequency shift is shown as a continuous line in Fig. S3B. The short-range force obtained from this frequency shift using the inversion procedure (10) is displayed in Fig. S3A as a continuous line. This force curve now exhibits the main feature of the experimental forces: a double well with similar force minimum values. Thus, this characteristic feature in the experimental short-range forces provides a conclusively indication that the system is actually evolving between two different bonding configurations during the approach and retraction cycle.

Another intriguing observation is the lost of imaging contrast after a vertical atom interchange process resulting in a Si deposition. As it can be seen in Fig. S1B, while the short-range force for the approach almost matches the retraction after the deposition of a Sn atom (inset of Fig. S1B), the instability giving rise to the Si deposition induced a drastic change in the tip apex so that the tip-surface force upon retraction is completely different than the force during the tip approach: the retraction curve now exhibits a single minimum, and the onset of the short-range interaction force, now appears 2.6\AA closer to the surface than for the approach curve.

Our simulations support that the onset of the short-range interaction at closer tip-surface sep-

aration observed for this new tip termination corresponds to a tip apex that has lost its outermost atom during the interchange, resulting in a metastable, blunted tip apex which yields a worse topographic contrast. In Fig. S4A, we present a comparison of the short-range force estimated for the retraction after a Sn deposition process (Figs. S1 and S3) together with the short-range force calculated for an approach of a blunted tip apex towards the surface. To obtain this force curve, we have removed the outermost atom of the tip model in Fig. 2, then we have relaxed it keeping fixed only the Si and H atoms in the top layer (see a general view of the tip apex and the surface model in Fig. S4B), and finally we have calculated an approach curve over the surface position at which the deposited Si atom is located, with identical tip initial position and tip-surface orientation for the fixed part of the tip (top most Si and H atoms) as for Fig. 2. Far from the surface, the tip apex looks quite blunt but when reaching the onset of the short-range interactions, atoms at the end of the tip relax, resulting in a significant tip sharpening (see the evolution of the bonding configuration and atomic relaxations in Fig. 4C). This sharpening of the tip apex gives similar maximum force values as in the experiments upon further approach towards the surface. At variance with the experiments, upon further reduction of the tip-surface distance using this simple tip model, the force becomes attractive again by the interaction of atoms on the second layer over the apex with Sn atoms surrounding the Si impurity.

Combining this sharpening of the tip at close tip-surface distances with lateral scanning might induce a reorganization of this metaestable tip apex (quite deformable but still capable of imaging with low atomic resolution) to a more stable tip termination that would restore the image contrast, as it is observed in the experiments.

2.4 Successive Sn deposition by vertical interchange atom manipulation

As we mention within the main text, there are tips that can produce vertical interchange atom manipulations alternatively depositing Sn and Si (see Figs. S1 and S2), others can only deposit Si atoms like in Fig. 3, and others only can deposit Sn atoms. An example of vertical interchange atom manipulations with a tip exclusively depositing Sn atoms, is shown in Fig. S5. In

the inset image on the left of Fig. S5A, there is an image of the Sn/Si(111)-($\sqrt{3} \times \sqrt{3}$)R30° surface containing three substitutional Si atoms, a defect with contrast in between Sn and Si corresponding to a dopant of the Si(111) substrate on the left, and two other defects at the bottom (2). In successive vertical interchange atom manipulations, the Si defects were replaced, one atom at a time, by Sn atoms coming from the tip, leaving the other defects at their original locations. It is remarkable the similarity of the frequency shift curves in these Sn deposition experiments with the corresponding curves for Sn depositions shown in Figs. S1 and S2.

2.5 Additional outcomes from similar force spectroscopy experiments: production of vacancies

When performing force spectroscopy over the Sn/Si(111)-($\sqrt{3} \times \sqrt{3}$)R30° surface exploring the repulsive part of the tip-surface short-range interaction force, we can obtain as an outcome of a vertical interchange atom manipulation either the deposition of Sn atoms (Fig. S1A) or the deposition of a Si atom (Fig. S1B). Another result we have experimentally observed is the production of a single vacancy instead of obtaining a vertical atom interchange.

The creation of a vacancy is shown in Fig. S6. In this experiment we applied the same protocol as for the vertical interchange atom manipulations shown in Fig. 1, observing frequency shift signals upon approach and retraction similar that of a Si deposition (Fig. 1B), and partially losing atomic contrast like in Fig. 1B. An image of the same surface area taken after restoring good atomic resolution revealed the formation of a vacancy instead of the deposition of a Si atom at the location of the targeted Sn atom. The topographic profiles shown in Fig. S6, reveal the difference between a substitutional Si defect and a vacancy. While the relative height between Sn and Si atoms approximately corresponds to the 0.5 Å predicted from first-principles calculations (3), the relative height difference between the vacancy and the Sn atoms is always higher than this value.

The probability of obtaining a vacancy as outcome of a vertical atom interchange process is, however, very low. Only a 9% of all the total vertical interchange atom manipulations we have performed in the Sn/Si(111) system resulted in the creation of a vacancy.

3 Concerted lateral interchange atom manipulation on the Sn/Si(111)-($\sqrt{3} \times \sqrt{3}$)R30° surface.

The creation of the atomic nano-structure shown in Fig. 3 was performed with a tip apex that only could deposit Si atoms. Upon the impossibility of removing Si substitutional defects from the surface by depositing Sn atoms from the tip, for the completion of these atomic patterns, we made use of an additional manipulation technique available for AFM: the concerted lateral interchange of atoms in the plane of a surface (18). In this manipulation method, the surface potential energy is modified very locally by the AFM tip proximity, so that the energy barriers for the concerted lateral interchange diffusion of surface atoms are lowered below a threshold in which this process can occur via thermally activated hopping of the atoms at room temperature (18). The Si atom beside the “i” character in Fig. 3M was put aside by applying several consecutive lateral interchange atom manipulations, and the nano-structure was finally completed.

These lateral interchange atom manipulations between Sn and Si atoms of the Sn/Si(111)-($\sqrt{3} \times \sqrt{3}$)R30° surface were carried out following the protocol described in Ref. 18, which is summarized in Fig. S7B. After the acquisition of the image shown in Fig. S7A, the scan size was reduced, the fast scan direction was set parallel to the line connecting the center of the adatoms to be manipulated, and the slow scan was stopped over this line —marked by a blue arrow in Fig. S7A. Successive line scans were performed at this surface location (lower half of the image in Fig. S7B) in the direction indicated by the arrows and progressively increasing the tip-surface interaction force and lifting the tip up approximately 1 Å in the way back. At a given threshold force, the lateral manipulation takes place (green arrow in the image in Fig. S7B), and the Si atom and its first neighboring Sn atom along the fast-scan direction interchanged their positions in a concerted way at the surface plane, as it is shown by the profiles. Finally, the slow scan was restored and the surface was imaged following a normal raster pattern (upper half of the image in Fig. S7B).

4 Experimental evidence of vertical interchange atom manipulation in other surfaces.

The work presented here focuses on vertical atomic interchange processes in the Sn/Si(111)-($\sqrt{3} \times \sqrt{3}$)R30° surface. However, in our thorough force spectroscopy study of this and other surfaces (6), we have identified these vertical interchange atom manipulations in other systems like the Pb/Si(111)-($\sqrt{3} \times \sqrt{3}$)R30° surface and the In/Si(111)-($\sqrt{3} \times \sqrt{3}$)R30° surface. Examples of vertical atom interchange processes in these surfaces are shown in Fig. S8.

As in the case of the Sn/Si(111), Si impurities in a perfect atomic layer of Pb (Fig. S8A) and In (Fig. S8B) grown on top of a Si(111) substrate appear as protrusions with a diminished contrast. In the upper panel on Fig. S8A, the Si atom pointed by an arrow in the image on the left was substituted by a Pb atom coming from the tip as it is shown in the image on the right. In the lower panel, a Pb atom was removed at the position indicated by the arrow in the image on the left, and as a result of a vertical interchange atom manipulation, a Si atom was deposited at the same location of the surface as can be identified by careful inspection of the image on the right. The line profile in Fig. S8A depicts the typical topography of the Pb/Si(111)-($\sqrt{3} \times \sqrt{3}$)R30° surface. This profile shows a curious behavior exhibited by Pb atoms that are partially surrounded by Si. The atom marked with an arrow in the profile is a Pb atom surrounded by three first neighboring Si atoms, and it presents a slightly lower topographic contrast than the Pb atoms far from any impurity, as we quantified in Ref. (6). Notice that in the same image, there are two additional Pb atoms surrounded by three Si atoms presenting similar slightly diminished contrast, and in the upper panel, similar behavior can be seen in Pb atoms surrounded by four and three Si atoms.

Figure S8B shows similar cases of In deposition (upper panels) and Si deposition (lower panels) produced by vertical atomic interchange processes between the AFM tip and the In/Si(111)-($\sqrt{3} \times \sqrt{3}$)R30° surface. The profile on Fig. S8B points out a characteristic of this surface that makes it different from the Sn/Si(111) and the Pb/Si(111) ones. This distinction is the considerable topographic height difference between In and Si atoms (that in the profile shown in Fig. S8B

is approximately 0.7 \AA) in contrast with the lower height difference seen in the Sn/Si(111) and the Pb/Si(111) systems.

Our hypothesis is that these vertical interchange atom manipulations at semiconductor surfaces using AFM might be a quite general phenomenon, that probably is going to be found in other surfaces having Si and Ge as support substrates, and it might be also found in other semiconductor surfaces of different nature.

References and Notes

1. T. R. Albrecht, P. Grütter, D. Horne, D. Rugar, *J. Appl. Phys.* **69**, 668 (1991).
2. S. T. Jemander, N. Lin, H. M. Zhang, R. I. G. Uhrberg, G. V. Hansson, *Surf. Sci.* **475**, 181 (2001).
3. Y. Sugimoto, *et al.*, *Phys. Rev. B* **73**, 205329 (2006).
4. M. Abe, Y. Sugimoto, O. Custance, S. Morita, *Appl. Phys. Lett.* **87**, 173503 (2005).
5. M. A. Lantz, *et al.*, *Science* **291**, 2580 (2001).
6. Y. Sugimoto, *et al.*, *Nature* **445**, 64 (2007).
7. H. Hölscher, *et al.*, *Phys. Rev. B* **64**, 075402 (2001).
8. F. J. Giessibl, *Phys. Rev. B* **56**, 16010 (1997).
9. U. Dürig, *Appl. Phys. Lett.* **75**, 433 (1999).
10. J. E. Sader, S. P. Jarvis, *Appl. Phys. Lett.* **84**, 1801 (2004).
11. P. Jelinek, H. Wang, J. P. Lewis, O. F. Sankey, J. Ortega, *Phys. Rev. B* **71**, 235101 (2005).
12. G. Mills, H. Jónsson, *Phys. Rev. Lett.* **72**, 1124 (1994).
13. G. Henkelman, G. Jóhannesson, H. Jónsson, *Methods for Finding Saddle Points and Minimum Energy Paths, in Progress on Theoretical Chemistry and Physics*. Pp. 269-300, Ed. S. D. Schwartz (Kluwer Academic Publishers, 2000).
14. N. Sasaki, M. Tsukada, *Jpn. J. Appl. Phys.* **39**, L1334 (2000).
15. R. García, R. Pérez, *Surf. Sci. Rep.* **47**, 197 (2002).
16. L. N. Kantorovich, T. Trevethan, *Phys. Rev. Lett.* **93**, 236102 (2004).
17. N. Oyabu, *et al.*, *Phys. Rev. Lett.* **96**, 106101 (2006).

18. Y. Sugimoto, *et al.*, *Nature Materials* **4**, 156 (2005).
19. M. Abe, *et al.*, *Appl. Phys. Lett.* **90**, 203103 (2007).

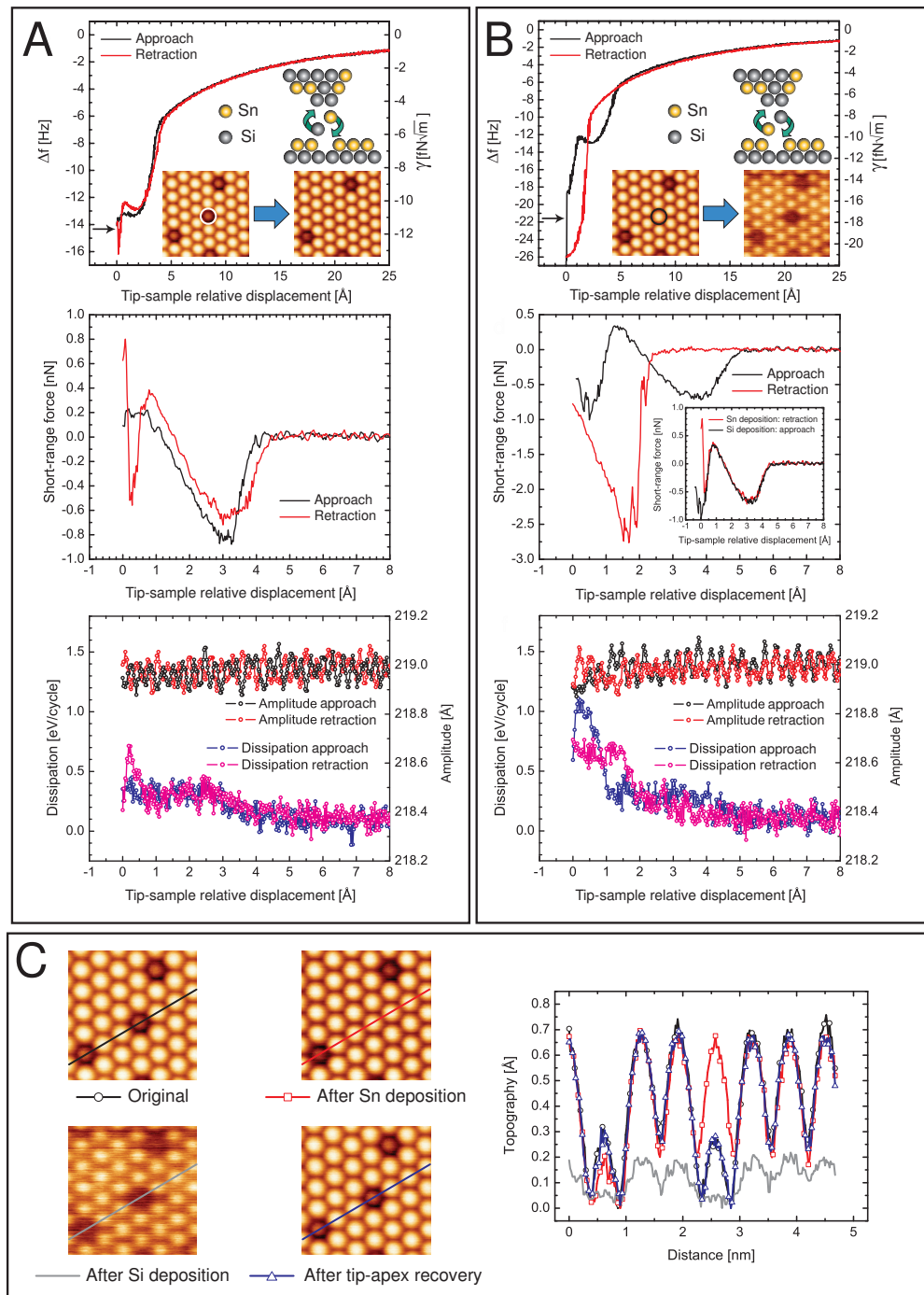


Figure S1. Force spectroscopic measurements associated with the manipulation processes shown in Fig. 1. **(A)** Frequency shift (Δf), short-range forces and dissipation signal simultaneously registered for the Sn deposition shown in Fig. 1A. **(B)** Variation of the same signals enumerated in (A) for the Si deposition displayed in Fig. 1B. The inset plot is a comparison of the corresponding short-range forces upon retraction in (A) and approach in (B). **(C)** Comparison of the topographic signal over the same surface location at different stages of the manipulations shown in Fig. 1. In the Δf plots, the corresponding normalized frequency shift (γ) (8) is displayed on the right axis. Acquisition parameters were: cantilever first mechanical resonant frequency (f_0) of 193738.0 Hz; cantilever oscillation amplitude (A) of 219 Å; cantilever stiffness (k) of 48.8 N/m; cantilever quality factor (Q) of 13000; a Δf set point value of -6.3 Hz is common to all the topographic images. Experiments were performed at room temperature.

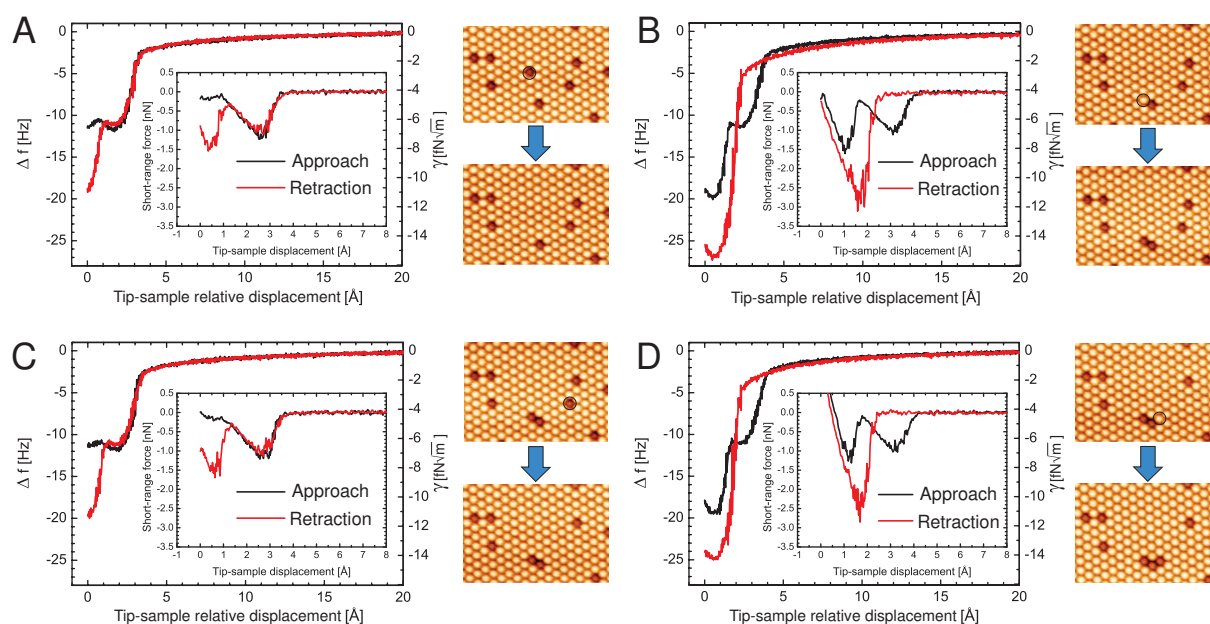


Figure S2. Reproducibility of alternate vertical interchange atom manipulations. **(A)** to **(D)** Variation of Δf as a function of the tip-surface relative displacement upon a single approach and retraction cycle in consecutive alternate depositions of Sn and Si atoms. The plot inside each graph corresponds to the tip-surface short-range interaction forces associated with the Δf curves displayed. The topographic images on the right side of each graph show the surface before (upper panel) and after (lower panel) the corresponding vertical interchange atom manipulation. A black circle marks the atom over which the curves were acquired keeping a lateral precision better than $\pm 0.1 \text{ \AA}$ (4, 19). In the Δf plots, the corresponding normalized frequency shift (γ) (8) is displayed on the right axis. Acquisition parameters were: $f_0 = 162299.7 \text{ Hz}$; $A = 219 \text{ \AA}$; $k = 28.7 \text{ N/m}$; a Δf set point value of -3.1 Hz is common for all the topographic images. Experiments were performed at room temperature.

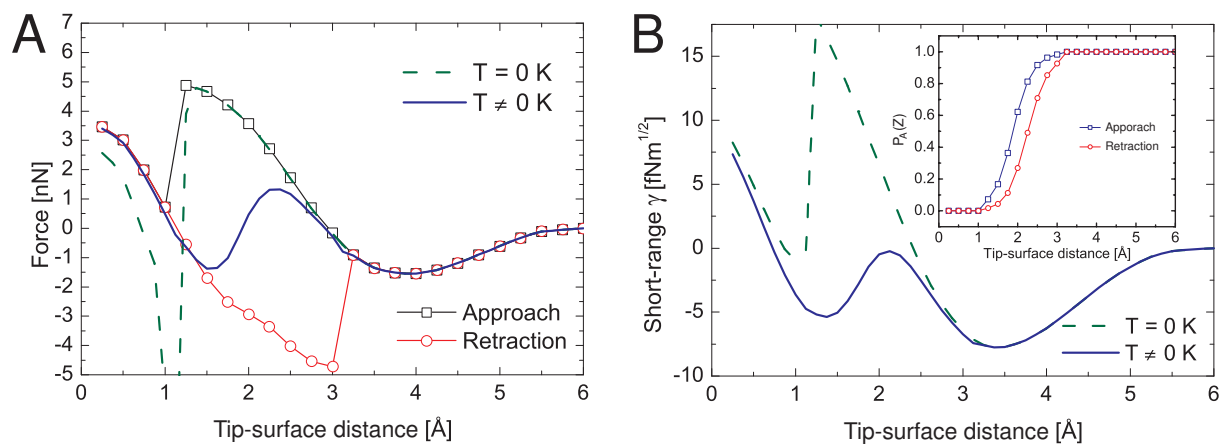


Figure S3. Theoretical short-range force curves. **(A)** Short-range forces associated with the evolution and transitions between the energy branches C and D of the system described in Fig. 2; squares and circles denote the force upon approach and retraction, respectively. The theoretical forces that would be obtained from the inversion of the frequency shift (the same procedure used in the experiments) at zero (dashed line) and room temperature (continuous line) are also depicted. **(B)** Normalized frequency shift (δ) obtained from the approach and retraction short-range force curves shown in (A), considering zero (dashed line) and non-zero temperature (continuous line). The inset displays the probability of being in the C branch during the approach-retraction cycle used to incorporate the effect of a non-zero temperature in the frequency shift calculation.

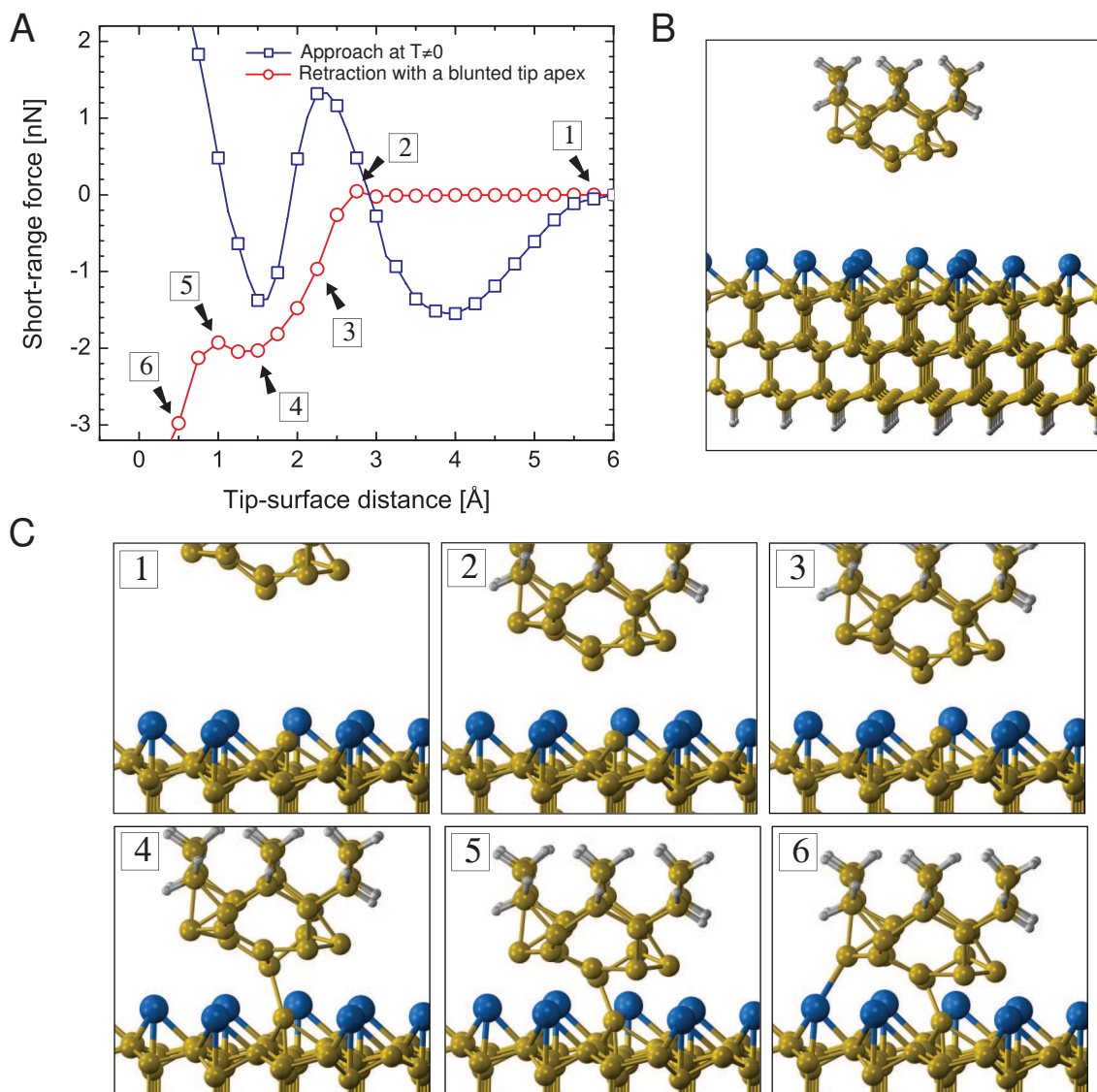


Figure S4. Theoretical force curves for a Si deposition. **(A)** Theoretical short-range force curves that simulate the experimental forces shown in Fig. S1B. The curve representing the approach (blue and squares) is the force curve obtained from the inversion procedure at a non-zero temperature shown in Fig. S3A. The retraction curve (red and circles) has been calculated by approaching a blunted tip model towards the surface. This tip corresponds to the stable, relaxed configuration found after removing the outermost apex atom in tip used in the rest of our simulations. The onset of the short-range chemical force is shifted $\sim 2.5\text{\AA}$ towards closer tip-surface distances, as it is clearly shown by the comparison with the approach force curve. **(B)** Ball-and-stick model of the initial atomic configuration used to calculate the retraction curve in (A). For this calculation, the atoms in the upper Si layer and the hydrogen atoms of the tip model are kept fixed. **(C)** Different stages of the bonding configuration at the tip-surface interface during the approach of the blunted tip model towards the surface; numbering corresponds to the numbers listed on the retraction curve in (A).

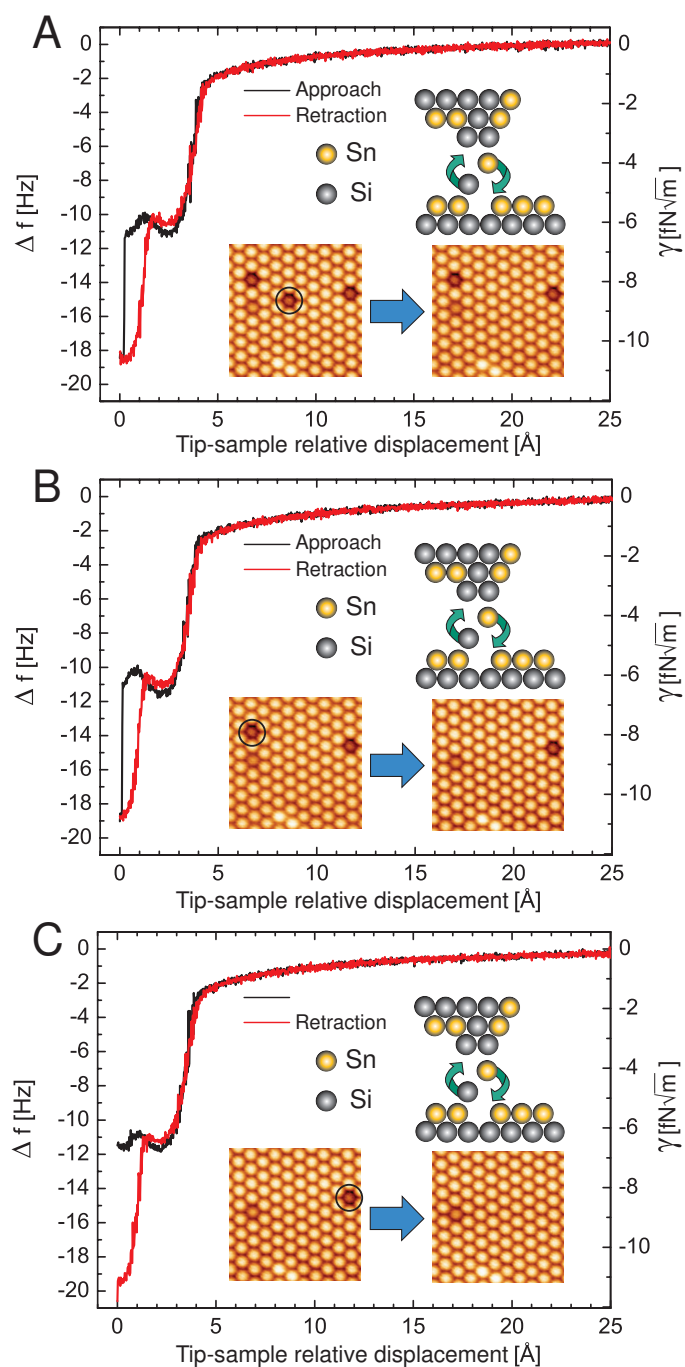


Figure S5. Successive vertical interchange atom manipulations resulting in the consecutive deposition of Sn atoms. (A) to (C) Variation of the Δf as a function of the tip-surface relative displacement upon approach and retraction in three consecutive replacements of surface Si atoms by Sn atoms coming from the tip. The topographic images inside each graph show the surface before (left) and after (right) the vertical interchange atom manipulation. A black circle marks the atom over which the curves were acquired, keeping a lateral precision better than $\pm 0.1 \text{ \AA}$ (4, 19). The normalized frequency shift (γ) (8) is displayed on the right axis of the corresponding Δf plot. The cartoon inside each image denotes the deposition of Sn atoms, following the color code described in Fig. 1 and bearing no further information about the tip-apex structure or composition during the experiments. Acquisition parameters were: $f_0 = 162299.7 \text{ Hz}$; $A = 219 \text{ \AA}$; $k = 28.7 \text{ N/m}$; image Δf set point values were -3.4 Hz for (A) and -3.7 Hz for (B) and (C). Experiments were performed at room temperature.

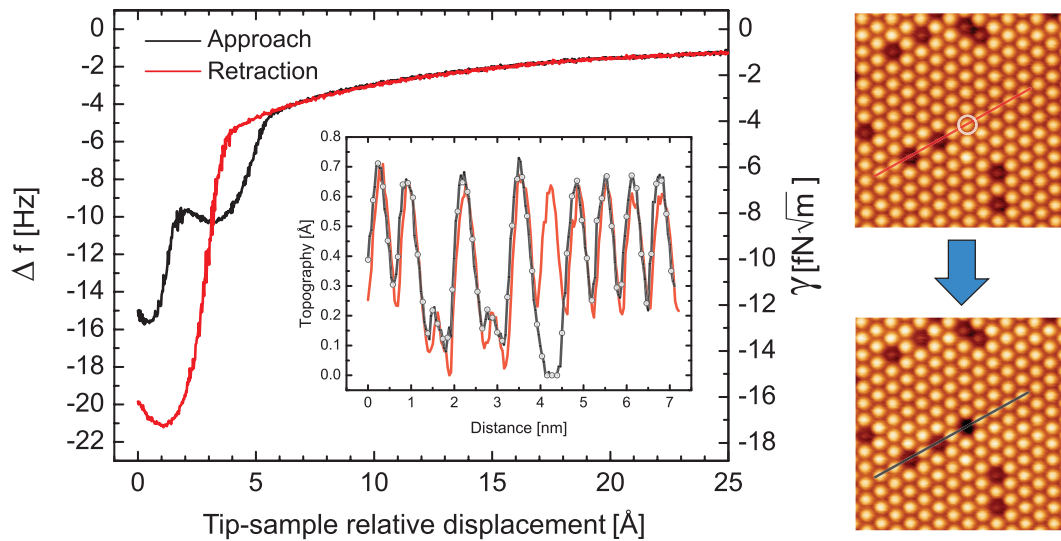


Figure S6. Creation of a surface vacancy. The graph shows the variation of the Δf signal as a function of the tip-sample relative displacement upon approach and retraction over the Sn atom marked with a white circle in the upper image on the right. As a result, a single atomic vacancy was created. The inset plot depicts the topography before (red) and after (black and symbols) the vacancy creation. The corresponding normalized frequency shift (γ) (8) is displayed on the right axis of the Δf plot. The creation of vacancies has considerably lower probability than the production of vertical atomic interchange processes (see the text). Acquisition parameters were: $f_0 = 193738.0$ Hz; $A = 219$ Å; $k = 48.8$ N/m; imaging Δf set point was -3.9 Hz. The experiment was performed at room temperature

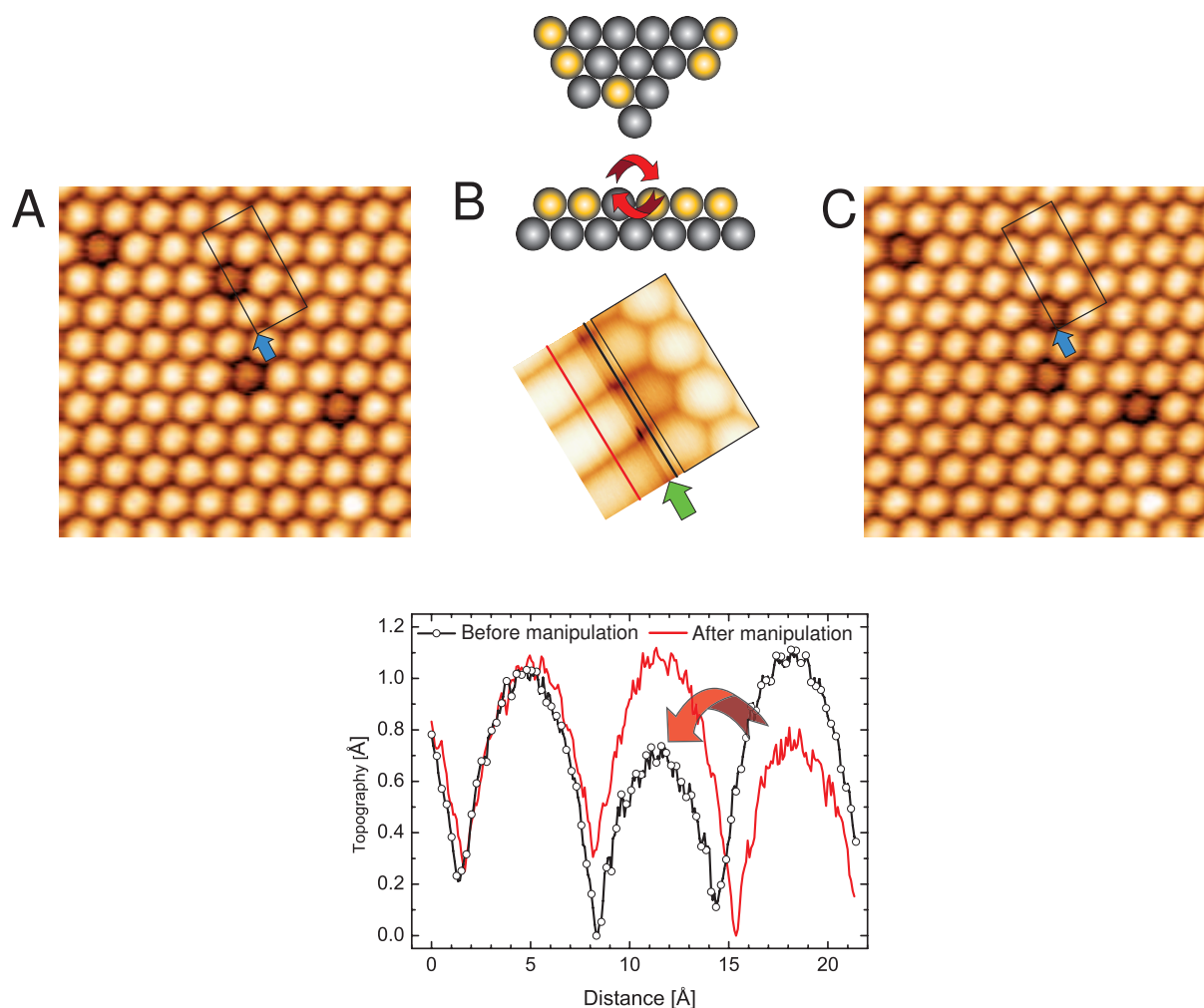


Figure S7. Concerted lateral interchange atom manipulation on the Sn/Si(111)-($\sqrt{3} \times \sqrt{3}$)R30° surface. (A) Topographic image of the surface area before the lateral manipulation. (B) Upper part: cartoon denoting lateral interchange atom manipulation. Center: topographic image showing the lateral interchange atom manipulation process. Lower part: profiles along the fast scan direction taken from the lower half of image in (B) that quantify the atomic corrugation before (black line with symbols) and after (red line) the lateral interchange manipulation. (C) Topographic image showing the manipulation result. The rectangles in (A), (B) and (C) mark the same surface area. Acquisition parameters were: $f_0 = 173993.1$ Hz; $A = 331$ Å; $k = 35.4$ N/m; Δf set point values for imaging and manipulating were -3.7 Hz and -5.0 Hz, respectively. Experiments were performed at room temperature.

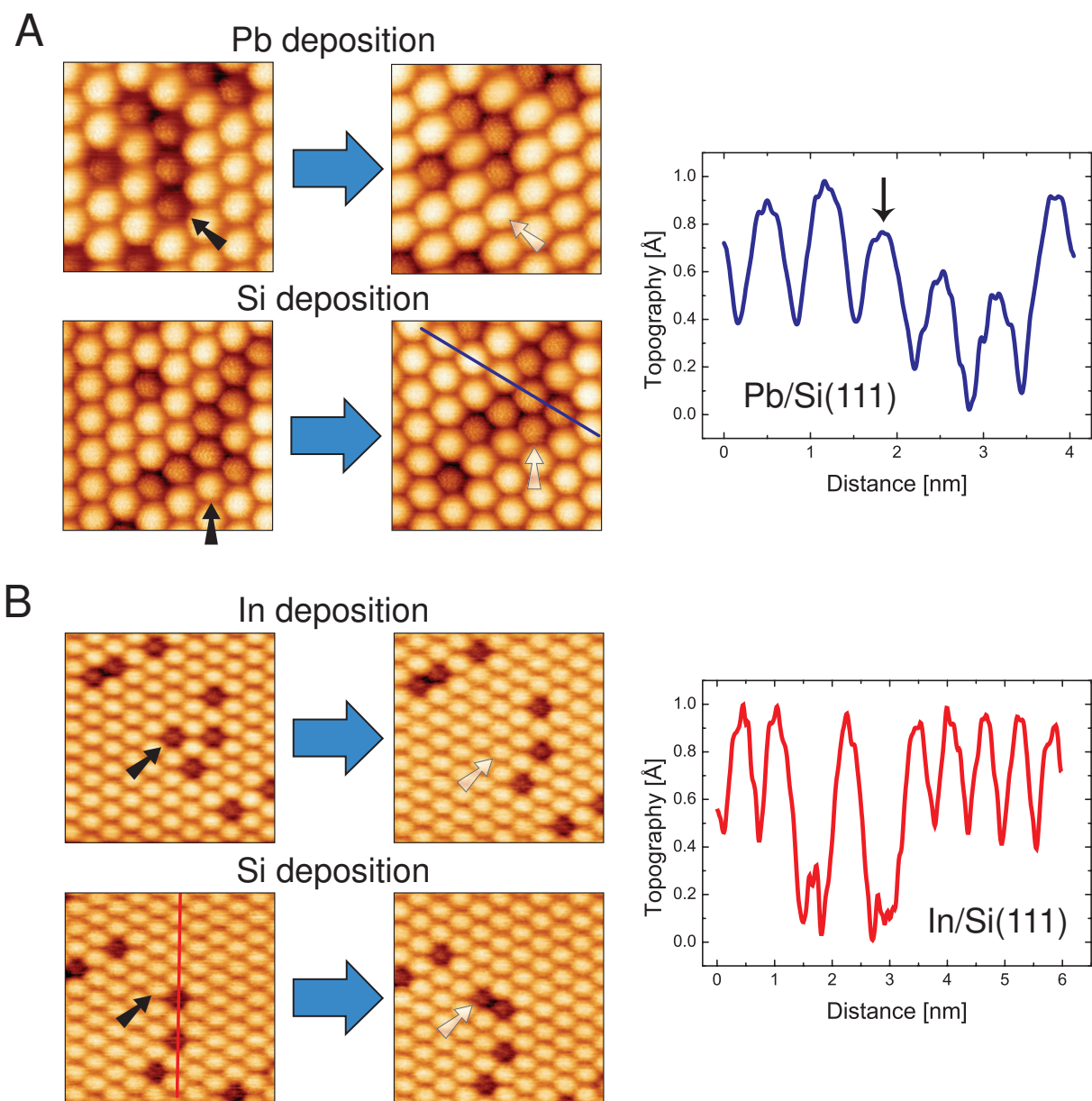


Figure S8. Vertical interchange atom manipulation in different surfaces than Sn/Si(111). **(A)** Vertical atom interchange processes on the Pb/Si(111)- $(\sqrt{3} \times \sqrt{3})R30^\circ$ surface. The upper panel displays a Pb deposition and the lower panel a Si deposition over the corresponding Si and Pb atoms marked with a black arrow in the images on the left; in the pictures on the right the same locations are pointed out with white arrows. Acquisition parameters were: $f_0 = 161688.6$ Hz; $A = 147$ Å; $k = 28.4$ N/m; Δf imaging set point value for all the images was -10.6 Hz. **(B)** Similar vertical interchange atom manipulations on the In/Si(111)- $(\sqrt{3} \times \sqrt{3})R30^\circ$, with a In deposition on the upper panel and a Si deposition of the lower panel over the corresponding Si and In atoms pointed out with an arrow in the images on the left. Acquisition parameters were: $f_0 = 166709.1$ Hz; $A = 300$ Å; $k = 31.1$ N/m; Δf imaging set point values were -3.4 Hz (upper left), -4.1 Hz (upper right), and -3.4 Hz (lower left) and -3.9 Hz (lower right). For both surfaces profiles are displayed on the right representing some intrinsic characteristics of the Pb/Si(111) surface (A) and the In/Si(111) surface (B), respectively (see the text for more details). In both cases, experiments were performed at room temperature.